Published in final edited form as:
*Sci Transl Med*. 2016 October 05; 8(359): 359ra131. doi:10.1126/scitranslmed.aag1424.

# Birefringence Microscopy Platform for Assessing Airway Smooth Muscle Structure and Function *in vivo*

**David C. Adams**[1,2], **Lida P. Hariri**[2,3,†], **Alyssa J. Miller**[1,†], **Yan Wang**[1,2], **Josalyn L. Cho**[1,4], **Martin Villiger**[2], **Jasmin A. Holz**[1,2], **Margit V. Szabari**[1,2], **Daniel L. Hamilos**[4], **R. Scott Harris**[1], **Jason W. Griffith**[1,4], **Brett E. Bouma**[2], **Andrew D. Luster**[4], **Benjamin D. Medoff**[1,4], and **Melissa J. Suter**[1,2,*]

[1]Division of Pulmonary and Critical Care Medicine, Massachusetts General Hospital, Harvard Medical School, Boston, MA 02114

[2]Wellman Center for Photomedicine, Massachusetts General Hospital, Harvard Medical School, Boston, MA 02114

[3]Department of Pathology, Massachusetts General Hospital, Harvard Medical School, Boston, MA 02114

[4]Center for Immunology and Inflammatory Diseases, Division of Rheumatology, Allergy and Immunology, Massachusetts General Hospital, Harvard Medical School, Boston, MA 02114, USA

## Abstract

The inability to visualize airway smooth muscle (ASM) cells *in vivo* is a major obstacle in understanding their role in normal physiology and diseases. At present, there is no imaging modality available to assess ASM *in vivo*. Confocal endomicroscopy lacks the penetration depth

---

[*]Author to whom correspondence should be addressed (msuter@mgh.harvard.edu).
[†]equal contribution

**Supplementary Materials**
Supplementary Methods on Processing Techniques and Experimental Arrangements

**Author Contributions:**
D.C.A. designed and performed experiments, developed technology, took part in clinical procedures, did image segmentation and data review, and wrote the manuscript. L.P.H. performed experiments and did image segmentation and data review. A.J.M. performed experiments, took part in clinical procedures, and did image segmentation and data review. Y. W. performed experiments and did image segmentation and data review. J.L.C. took part in clinical procedures and did image segmentation and data review. M. V. contributed to the development of technology. J.A.H. and M.V.S. took part in clinical procedures and did image segmentation and data review. D. L. H., R. S. H., and J.G. performed clinical procedures. B.E.B. developed technology. A.D.L. and B.D.M. took part in clinical procedures, wrote the manuscript, and supervised the clinical studies. M.J.S. designed experiments, developed technology, took part in clinical procedures, did image segmentation and data review, wrote the manuscript, and supervised the project.

**Competing Interests:**
The following patents and patent applications are relevant to the work presented in this manuscript.
Currently unlicensed MGH owned patent applications [M.J.S., D.C.A.]
WO2015084964 A1 “Compensating for Input Polarization Mode Variations”
PCT Application No. 15/100,815 “Apparatus and Method to Compensate for Input Polarization Mode Variation”
MGH owned patents licensed to NinePoint Medical [B.E.B]
US 7969578 B2 “Method and apparatus for performing optical imaging using frequency domain interferometry”
US 7995627 “Process and apparatus for a wavelength tuning source”
US 7742173 B2 “Methods, arrangements and systems for polarization-sensitive optical frequency domain imaging of a sample”
M.J.S., M.V, B.E.B are authors on additional MGH owned patents licensed to NinePoint Medical.
M.J.S and B.E.B have received sponsored research support from NinePoint Medical. M.J.S has received sponsored research support from Boston Scientific. M.J.S and B.E.B are consultants for NinePoint Medical.

and field of view, and conventional optical coherence tomography (OCT) does not have sufficient contrast to differentiate ASM from surrounding tissues. We have developed a birefringence microscopy platform which leverages the micro-organization of tissue to add further dimension to traditional OCT. We have utilized this technology to validate ASM measurements in ex vivo swine and canine studies, visualize and characterize volumetric representations of ASM *in vivo*, and to quantify and predict ASM contractile force as a function of optical retardation. We provide *in vivo* images and volumetric assessments of ASM in living humans and document structural disease variations in subjects with mild asthma. The opportunity to link inflammatory responses to ASM responses, and to link ASM responses to clinical responses and outcomes could lead to an increased understanding of diseases of the airway and ultimately to improved patient outcomes.

## Introduction

Asthma, a chronic inflammatory disease associated with airway remodeling and airway hyperresponsiveness (AHR), is estimated to affect more than 25 million individuals in the United States alone. The high prevalence and morbidity associated with asthma directly translates to a large economic burden to healthcare systems. During an acute asthma exacerbation, excessive bronchoconstriction occurs as a result of airway smooth muscle (ASM) activation (1). The mechanisms regulating ASM contraction are not clearly understood, although the magnitude of the response appears to be intimately linked to underlying inflammation (1). Over time, the airway remodels in asthmatics resulting in a significant increase in the thickness of the bronchial wall due in part to thickening of the ASM through hyperplasia and hypertrophy (2). This increase in ASM may further intensify bronchoconstriction and compromise lung function. Recent reports have suggested that ASM remodeling plays a key role in asthma control even in non-severe asthma (3), yet the ability to assess this remodeling process and determine the severity, spatial heterogeneity, natural history, and ultimately the influence of ASM remodeling on airway hyperresponsiveness in patients is currently unachievable. Much of what we know of asthmatic ASM is from biopsy or autopsy studies. Biopsy of ASM has been shown to provide greatly varying results (4), and assessment of ASM at autopsy only provides a single snapshot in time. In addition, although extensive literature exists detailing the thickening of ASM in asthmatic lungs as assessed through these types of histological studies (5, 6), little attention has been given to the broad morphological alterations engendered by the disease due to the difficulty associated with observing such changes.

The ability to comprehensively visualize ASM in patients over time may have a profound impact on understanding the development and progression of asthma. It may also serve as an important biomarker for asthma phenotyping and for guiding and monitoring therapeutic decisions. Patients with significant ASM thickening may benefit from bronchial thermoplasty, a new therapeutic ablative tool that targets ASM in order to ameliorate AHR and ultimately relieve asthma symptoms (7). However, carefully selecting patients with significant baseline ASM remodeling will likely be necessary to optimize patient benefit. In recent years, advances in our understanding of the immunological processes involved in asthma have resulted in the development of new biological agents for targeted therapy, though the reported success of these agents varies greatly likely due to non-specific patient selection and insufficient endotyping. It is clear that understanding the regulation of ASM function and linking this information to the underlying immunologic processes is a critical unmet need in advancing our understanding of asthma, targeting treatment, and improving patient care. The ability to image ASM structure and function in patients is pivotal to establishing this link.

Unfortunately, no method exists to visualize and directly measure ASM structure and function within a living patient. High resolution computed tomography (HRCT) imaging does not have sufficient resolution to discern layers of the airway wall, and confocal endomicroscopy lacks the necessary penetration depth to reach the ASM layer. Researchers have attempted to utilize endobronchial optical coherence tomography (OCT) with limited success. The resolution and depth of penetration of OCT is within the specifications necessary to image ASM fiber bundles several tens of microns in thickness; however, the intensity of light backscattered from the ASM is not significantly different from other surrounding mucosal tissues and therefore does not provide sufficient contrast for reliable ASM isolation. As a result of these limitations, efforts to use imaging techniques to assess ASM function have been restricted to measurements involving airway wall thickness and size (8–10).

Although OCT relies on the amount of backscattered light from the tissue, there is a wealth of additional information encoded in the returning light that may be used to extract details on the micro-structural and -mechanical tissue properties. Tissue form birefringence is the quantifiable anisotropy of ordered structures, such as smooth muscle fiber bundles, manifested in the differential propagation time of orthogonal polarization states of light transmitted through the tissue. Studies have demonstrated the potential of polarization sensitive OCT (PS-OCT) for estimating collagen and smooth muscle content in cadaverous aortas by assessing bulk tissue birefringence. However these studies were not able to discriminate between the tissue types and only provided an estimate of bulk collagen and smooth muscle content (11). We have developed a functional birefringence microscopy platform that, based on principles of polarimetry, generates both orientation resolved OCT (OR-OCT) and mechano-microscopy images (Fig. 1). OR-OCT dramatically increases the contrast of OCT by enabling the accurate extraction of the orientation of the birefringent tissue elements, which can be leveraged to isolate the ASM fibers given their inherent organization into bundles that surround the airway. Mechano-microscopy provides a non-invasive and non-contact imaging means of directly quantifying the ASM contractile force *in vivo*. In this study we demonstrate the superior accuracy of OR-OCT for quantifying ASM volume as well as the validation of the complementary mechano-microscopy for measuring the contractile force. We have additionally translated the birefringence microscopy platform into the clinic to assess ASM in healthy volunteer and asthmatic subjects, allowing us to quantify ASM fiber morphology and the effects of airway remodeling in asthma. The ability to comprehensively image ASM structure and function *in vivo* could be paradigm shifting in how we study asthma and other diseases involving the airways, and may also serve as a critical biomarker to more accurately phenotype patients, and guide therapeutic management.

## Results

We quantitatively assessed ASM mass in bronchial segments from freshly excised swine and canine specimens and validated the results against histopathology. We additionally investigated ASM remodeling metrics as a potential biomarker for asthma in human volunteers. All imaging was conducted using a custom, in-house developed functional birefringence microscopy platform that enabled the visualization of ASM structure through novel OR-OCT processing techniques, and of ASM function through mechano-microscopy. Images were acquired via both a catheter-based imaging and a bench-top microscope. Structural (intensity based) cross sections were displayed in real time, with the birefringence maps and volumetric reconstructions computed in post-processing.

### Orientation Resolved Optical Coherence Tomography (OR-OCT) for Imaging Airway Smooth Muscle

ASM plays a critical and multifaceted role in asthma. It is organized into bundles that wrap circumferentially around the airway and once activated, cause airway narrowing and bronchoconstriction. Regardless of the bronchomotor tone, ASM is birefringent due to its highly ordered structure. By isolating the circumferentially oriented (+/− 30°) birefringence signal we are able to distinguish ASM from adjacent birefringent tissues including collagen in the lamina propria (Fig. 2). This anisotropy is encapsulated in the calculation of the tissue's optic axis (OA), which corresponds to the polarization orientation for which the propagation time of light is minimized. OR-OCT allows us to accurately assess the circumferential and longitudinal tissue OA components through the inclusion of polarization-diverse light detection methods (see Supplementary Materials). In our OR-OCT images highlighting the ASM OA values outside of +/− 30° with respect to the circumferential orientation were excluded. This range was chosen to encompass the range of ASM fiber bundle orientation angles previously reported (12).

With fiber-optic based imaging, and especially in situations where a rotating fiber-optic catheter is employed, establishing absolute tissue orientation is rendered non-trivial by the scrambling of polarization states that occurs when the signal propagates through the optical fiber. To address this difficulty we have developed a means of obtaining information about the tissue orientation that utilizes the birefringence of the catheter sheath housing the imaging optics (Figs. S1 and S2, and Supplementary Materials). We have validated this technique using rubber phantoms (Fig. S3) and in biological tissue (Fig. S4). In addition to anisotropic isolation of the ASM fiber bundles, several data processing techniques were employed to more accurately represent the data depicted here. These include spectral binning of the polarization data (13) to reduce the impact of polarization mode dispersion (14), as well as novel techniques for filtering and circularizing the data (Fig. S5 and Fig. S6, respectively). All OCT images were circularized or rescaled using a uniform refractive index of n=1.35 for tissue, and n=1 for air. The value n = 1.35 was chosen as it corresponds to the mean refractive index of soft tissue at our system's central wavelength of 1310nm (15).

To demonstrate the accuracy of OR-OCT for assessing ASM structure using our birefringence microscopy platform, we conducted an *ex vivo* study using freshly excised canine (Fig. 3A, B) and swine (Fig. 3C, D) bronchi. Blinded assessments of ASM area calculated by independent readers on the OR-OCT and the alpha smooth muscle actin stained histology pairs were found to be highly correlated, $R^2 = 0.91$ (Fig. 3E). Considered separately, the 80 paired images for the canine assessments had an $R^2$ of 0.81, whereas the 82 paired swine images had an $R^2$ of 0.92. We attribute the reduced correlation calculated in the canine samples to the delay from animal sacrifice to imaging, resulting in increased tissue degradation, which is known to have a deleterious effect on image fidelity (16). A Bland-Altman analysis was performed to assess the agreement between the OR-OCT measures of ASM against those obtained from the matched histology slides (Fig. 3F). The results reveal a high concordance with minimal bias (Bias: −0.02 $mm^2$; 95% CI: −0.277 $mm^2$, +0.236 $mm^2$). We additionally observed that compared to swine bronchi, which possess clean, ordered tissue layers with minimal perichondria, canine bronchi appeared more irregular, with an increased abundance of both ASM and perichondrial tissue, particularly in the more distal airways, similar to human airways.

## In vivo Assessment of ASM Remodeling in Asthma Patients

To provide some insight into the morphological changes associated with asthma and to demonstrate the potential role of OR-OCT in monitoring these changes, we performed *in vivo* imaging on subjects with mild allergic asthma and on healthy controls (see Supplementary Materials Table 1 for subject characteristics). Sub-segmental bronchi of comparable diameter located in the right upper lobe were imaged and the ASM morphology was assessed to determine differences between the two groups (Fig. 4). To enhance the visibility of ASM remodeling in asthma through hyperplasia and hypertrophy, we have parameterized the volumetric reconstructions and en face views by encoding ASM thickness in color (see Supplementary Materials for more details).

Using the thickness-encoded volumetric data it is possible to both visualize and quantify the morphological ASM remodeling changes that are present in the asthmatic airway. To do this we assessed the ASM fiber band width and thickness within the airways of six volunteer subjects *in vivo* (n=3 asthmatic and n=3 healthy controls). 6 mm longitudinal segments of equal airway diameter (+/− 0.1 mm) were assessed in each of the study participants. Segments were chosen that were free from airway bifurcations or excessive mucus. Representative longitudinal reslices from airway sections obtained from a non-asthmatic healthy control (Fig. 4E) and from an asthmatic subject (Fig. 4F) demonstrate the identification of ASM band peaks as well as ASM band widths. These parameters were averaged for each subject for comparison between the asthmatic and healthy control groups (Fig. 4G and Fig. 4H). The measured values for ASM thickness (healthy controls: 35.90 μm, SD = 4.28, asthmatic subjects: 70.30 μm, SD = 14.70 for) are consistent with previously published results (healthy controls: 20–24 μm, asthmatic subjects: 40–88 μm) (18, 19).

## Dynamic Assessment of ASM Contractile Force using Mechano-Microscopy

Though ASM remodeling is known to occur in asthmatic subjects, little is known about the functional consequences of this remodeling and how it affects AHR. Of particular interest is determining if asthmatic ASM cells are themselves hyper-contractile, or if the AHR observed in asthmatics is solely a result of an increase in ASM volume and the interaction with inflammatory cells.(20) The ability to not only assess ASM structure but also to assess

ASM function in patients *in vivo* could potentially be instrumental in increasing our understanding of the functional aspects of asthma, in guiding patient management, and in assessing the therapeutic response. Using mechano-microscopy we demonstrate that we can precisely estimate the force of contraction of the ASM based on the birefringence signature.

Optical retardation can be associated with the density and degree of order of the birefringent elements (21, 22). Previous work using polarized light microscopy found that the bulk birefringence of excised ASM strips increased during muscle contraction (23, 24). Though interesting, this approach offered no viable pathway for studying ASM contraction *in vivo*. To assess muscle contraction, our birefringence microscopy platform was set up in a bench-top microscope configuration for imaging sections of trachea, including the trachealis muscle, from swine. Airway segments were mounted onto an isometric force transducer and contraction was stimulated using methacholine. During contraction the exerted force was measured concurrently with image acquisition (Fig. S7). Analysis of the isolated ASM local retardation and the measured force of contraction yielded a consistently linear relationship ($R^2 = 0.942$), providing strong evidence that the retardation of the ASM fibers can be associated with a change in stress induced on the fibers (Fig. 5). The force transducer measures the force exerted by the entire sample, and as a result the measured force is dependent on the transverse (out of plane) cross-sectional area of ASM in the sample while the imaging plane is oriented along the circumferential axis (with a transverse thickness of approximately 25 μm, determined by the beam waist at the focus). To compare the ASM contractile force and measured local retardation between samples we estimated the average cross-sectional ASM area in each and corrected for the difference (Fig. S8, Supplementary Materials text, and Materials and Methods). In establishing this relationship we assumed that the trachealis muscle acts only in the circumferential direction. Correcting for the area of ASM resulted in close agreement between the samples, yielding a mean mechano-microscopy coefficient of $1.558\times10^3$ g•μm/(deg•$\mathrm{cm}^2$) (Fig. 5D).

To establish the translatability of these results to an *in vivo* setting, we conducted mechano-microscopy imaging to investigate changes in birefringence observed during contraction using clinically viable bronchoscopic catheters. Volumetric imaging of an *ex vivo* segment of swine bronchus (5.0 mm in diameter) was performed at two separate time points corresponding to the at-rest and contracted states following the application of methacholine (Fig. 6). The pre- and post-methacholine datasets were analyzed and airway area, ASM thickness, and ASM local retardation were quantified. By comparing the two airway states we calculated for the contracted state a decrease in airway lumen diameter of 9.0%, a minute decrease in ASM thickness of 0.9% (possibly due to strain-induced compression balancing the reduction in ASM circumference), and an increase in ASM local retardation of 73.4%. Using the ASM volume-adjusted relationship between local retardation and stress that we obtained from the previous experiment we calculated a total pressure exerted during contraction of the airway segment to be 17.4 $\mathrm{cmH_20}$. This predicted pressure value appears consistent with previously reported results obtained from swine bronchial segments in response to acetylcholine (25) given the airway narrowing observed (26).

## Discussion

Through the development of our birefringence microscopy platform together with novel processing techniques we were able to synergistically image and assess ASM structure and physiologic function in human subjects for the first time. This is achieved by utilizing the optical orientation of birefringent tissue to generate OR-OCT images of ASM, and the local retardation to assess the contractile force through innovative mechano-microscopy techniques. We additionally devised novel calibration algorithms to ensure the compatibility with our standard clinical endobronchial OCT catheters, enabling OR-OCT and mechano-microscopy imaging to be employed *in vivo* during bronchoscopy procedures, with minimal additional demands placed on the clinician or patient.

Quantification of ASM structure and function will likely emerge as key component in the assessment of asthma. Asthma often presents a therapeutic challenge to clinicians. Endotypes of asthma have been shown to respond differently to therapeutics, as has been demonstrated in clinical trials assessing immunomodulatory agents (27). Likewise, asthmatic patients presenting with increased ASM thickness have shown increased response to bronchial thermoplasty (28, 29), further suggesting that ASM may serve as critical biomarker for therapeutic decision-making. The potential to link ASM mass, activation state and bronchomotor tone to the underlying inflammatory process that likely drives asthma pathogenesis will be a major advance. We have begun to do this by utilizing our birefringence microscopy platform to study the differences in the airways of allergic patients with and without asthma. We have found that patients with mild allergic asthma have markedly increased ASM mass compared to allergic patients without asthma and to healthy controls (see Cho J.L., et al., co-submitted manuscript). Allergic subjects without asthma had ASM comparable to healthy controls. This is notable as it suggests a fundamental difference in ASM even in mild asthmatics. Understanding what drives this difference in ASM and what mediates ASM contraction in asthma will be a major advance in our understanding of asthma pathogenesis and is now approachable using birefringence microscopy in conjunction with detailed characterization of the airway immune and inflammatory response.

The implications of this technological advancement in enabling the *in vivo* assessment of ASM structure, and perhaps more importantly function, will likely extend beyond asthma and will be useful in assessing ASM structure and function in other airway based diseases, such as COPD and cystic fibrosis, and to other organ system such as the gastrointestinal tract or cardiovascular system where smooth muscle cells play an integral role in physiological function. The robustness, nonionizing and relatively noninvasive nature of this platform enables immediate clinical implementation, which will provide unprecedented details of airway structure and function not offered by existing technologies.

## Materials and Methods

### Study Design

The purpose of this study was to investigate the ability of our birefringence microscopy platform to assess ASM distribution and function. The study was divided into a series of experiments. In the first experiment, swine and canine airways were imaged *ex vivo* and the ASM areas were measured and compared to histology. A total of 162 matches were assessed for ASM areas, with the histology and cross-sectional images assessed by two independent blinded readers. The next experiment involved volumetric imaging of 3 asthmatic and 3 non-asthmatic individuals, randomly selected. In this experiment the volumetric ASM distributions were compared between the two groups using semi-automated quantification algorithms. Finally, *ex vivo* imaging was performed during muscle contraction and the change in birefringence was related to the force of muscle contraction. The calculated birefringence-force parameter was then used to estimate the pressure exerted during the contraction of a segment of a swine airway.

## Birefringence Microscopy Imaging System

The system we used for all imaging data presented was a custom built microscopy platform based on OCT. Polarization sensitivity was achieved by inter A-line modulation producing birefringence maps comprised of half the number of A-lines per frame as the intensity-based images. A-lines in the birefringence images were then doubled so the horizontal pixel count matched that of the intensity-based images. The image acquisition rate was 33 frames per second for 2048 (intensity) A-lines per frame, with real time images displayed at ~6 frames per second. A schematic of the system is presented in figure 1 and a detailed description of the system components, image processing and display can be found in the text of the Supplementary Materials section.

## Ex Vivo Canine and Swine Bronchi Imaging Procedure

Swine lungs were obtained from the Massachusetts General Hospital Knight Surgical Labs within 1–2 hours of sacrifice. Seventeen airway segments ranging in diameter from 3–7 mm and in length from 1–2 cm were imaged using the endoscopic birefringence microscopy platform. Freshly excised canine lungs were obtained from Boston Scientific Corporation, where they were immersed in HEPES buffered saline (Sigma Aldrich) and shipped to our laboratory overnight. Nineteen canine airway segments, ranging in diameter from 2–5 mm and a length of 1–2 cm were also imaged.

To prepare the segments for imaging, they were dissected from the lung and placed on cotton gauze. A saline flush was then performed to clear the airway of any blood that was present as a result of the dissection and the imaging catheter was placed within the airway segment. The imaging catheter pullback rate for all of the excised airway segments was 0.5 mm/s, corresponding to an image-to-image pitch of approximately 15 μm.

## Histology and ASM Correlation

Imaged airway segments were fixed in formalin for 48 hours and submitted for histology. Approximately 10 evenly spaced histology sections were cut from each airway segment. Of the 10 sections, 5 were selected for matching that adhered to the following criteria: closed airway free of side branches; intact epithelium; little to no tissue processing artifacts. Each slide selected was matched to a corresponding OCT frame. Both H&E (for matching) and polyclonal rabbit anti-α smooth muscle actin (αSM-actin; Abcam), for assessing ASM, stains were digitized using a Nanozoomer 2.0RS (Hamamatsu Corp.) at 5× magnification.

Manual segmentation of the ASM and computation of the associated ASM area was performed on both the OR-OCT and the corresponding digitized histology slides in ImageJ (National Institute of Health), by two independent blinded readers.

## Local Retardation Correlation with ASM Contractile Force

Fresh swine tracheas were obtained from swine sacrificed in the Massachusetts General Hospital Knight Surgical Labs. To image the trachealis muscle, a tracheal ring approximately 5mm in length was dissected from the trachea and from this ring a section extending several mm beyond either edge of the trachealis muscle was further dissected. The lengths of the muscle bundles were approximately 1 cm, with a width of 2 mm. The thickness of the muscle was estimated from the imaged cross-section and varied slightly from sample to sample. Prior to imaging, the tissue was allowed to equilibrate for one hour in a Krebs-Henseleit buffered solution maintained at 37°C and a pH of 7.4.

The tracheal section was mounted to the force transducer setup and a baseline tension of approximately 10% above resting tension was applied. To assess the contractile response to methacholine a 1 mL saline solution of methacholine ($10^{-1}$ M) was applied to the tissue lumen with a syringe in order to stimulate contraction while imaging. The resultant local retardation data was averaged over 5 second intervals for smoothness and clarity. For additional details regarding the force measurement setup see Supplementary Materials.

## Volumetric Imaging of Swine Airway Segment at Relaxed and Contracted States

Swine lungs were obtained as previously described and a segment 2.7 cm long with an average inner diameter of 5 mm (as measured from structural OCT images) was equilibrated in a Krebs-Henseleit solution and placed horizontally on cotton gauze. The imaging catheter was centered in the segment and volumetric imaging at a pullback rate of 1 mm/s was performed 5 seconds following the application of 1 mL of methacholine ($10^{-1}$ M) to the luminal and outer surfaces of the segment, and again 3 minutes after contraction had begun. ASM isolation and thickness calculations were accomplished according to the procedures laid out in Supplementary Materials. To determine the exerted pressure as a result of the ASM contraction, the volume of ASM was calculated and the previously determined mechano-microscopy coefficient for swine ASM was applied. The total exerted force was subsequently converted to pressure according to standard equations used in the calculation of the circumferential stress of a thin-walled cylinder subject to internal pressure (see Supplementary Materials).

## Imaging Human Volunteers During Bronchoscopy

This study was approved by the Massachusetts General Hospital Institutional Review Board. Informed consent was obtained from all subjects. Study participants underwent baseline pulmonary function testing with methacholine to determine asthma status according to the American Thoracic Society criteria for the diagnosis of asthma (30). Subject characteristics are included in Table S1. Shortly after baseline testing a bronchoscopy procedure was performed at which time OR-OCT images were collected by advancing the imaging catheter through the bronchoscope access channel. 3 cm long airway segments were imaged in 30 seconds. All imaging locations included in this manuscript were obtained from subsegmental bronchi located in the right upper lobe. Details outlining the methods used for determining the ASM thickness and band parameter calculations can be found in the Supplementary Materials.

### Statistical Analysis

Statistical analyses were performed using GraphPad Prism (version 6). Arithmetic means were compared using two-tailed $t$ tests, with $P$ values less than 0.05 considered statistically significant.

## Supplementary Material

Refer to Web version on PubMed Central for supplementary material.

## Acknowledgments

**Funding:** This work was supported in part by the US National Institutes of Health (R01CA167827 awarded to M.J.S) and in part by Boston Scientific Corporation (2014A050616 awarded to M.J.S). B.E.B and M.V were supported by the US National Institutes of Health (EB105903 awarded to B.E.B). The clinical studies were supported by the US National Institutes of Health (U19AI095261 and R37AI040618 awarded to A.D.L).

## References and Notes

1. Bosse Y. Asthmatic airway hyperresponsiveness: the ants in the tree. Trends in molecular medicine. 2012; 18:627–633. [PubMed: 23062358]
2. Pepe C, Foley S, Shannon J, Lemiere C, Olivenstein R, Ernst P, Ludwig MS, Martin JG, Hamid Q. Differences in airway remodeling between subjects with severe and moderate asthma. J Allergy Clin Immunol. 2005; 116:544–549. [PubMed: 16159622]
3. Girodet PO, Allard B, Thumerel M, Begueret H, Dupin I, Ousova O, Lassalle R, Maurat E, Ozier A, Trian T, Marthan R, Berger P. Bronchial Smooth Muscle Remodeling in Nonsevere Asthma. Am J Respir Crit Care Med. 2016; 193:627–633. [PubMed: 26540234]
4. Labonte I, Laviolette M, Olivenstein R, Chakir J, Boulet LP, Hamid Q. Quality of bronchial biopsies for morphology study and cell sampling: a comparison of asthmatic and healthy subjects. Canadian respiratory journal : journal of the Canadian Thoracic Society. 2008; 15:431–435.
5. Carroll N, Elliot J, Morton A, James A. The structure of large and small airways in nonfatal and fatal asthma. The American review of respiratory disease. 1993; 147:405–410. [PubMed: 8430966]
6. Bara I, Ozier A, Lara JM Tunon de, Marthan R, Berger P. Pathophysiology of bronchial smooth muscle remodelling in asthma. The European respiratory journal. 2010; 36:1174–1184. [PubMed: 21037369]
7. Castro M, Rubin AS, Laviolette M, Fiterman J, Lima M De Andrade, Shah PL, Fiss E, Olivenstein R, Thomson NC, Niven RM, Pavord ID, Simoff M, Duhamel DR, McEvoy C, Barbers R, Hacken NH Ten, Wechsler ME, Holmes M, Phillips MJ, Erzurum S, Lunn W, Israel E, Jarjour N, Kraft M, Shargill NS, Quiring J, Berry SM, Cox G, A. I. R. T. S. Group. Effectiveness and safety of bronchial thermoplasty in the treatment of severe asthma: a multicenter, randomized, double-blind, sham-controlled clinical trial. American journal of respiratory and critical care medicine. 2010; 181:116–124. [PubMed: 19815809]
8. LaPrad AS, Szabo TL, Suki B, Lutchen KR. Tidal stretches do not modulate responsiveness of intact airways in vitro. Journal of applied physiology. 2010; 109:295–304. [PubMed: 20431023]
9. Noble PB, West AR, McLaughlin RA, Armstrong JJ, Becker S, McFawn PK, Williamson JP, Eastwood PR, Hillman DR, Sampson DD, Mitchell HW. Airway narrowing assessed by anatomical optical coherence tomography in vitro: dynamic airway wall morphology and function. Journal of applied physiology. 2010; 108:401–411. [PubMed: 19910337]
10. Ansell TK, McFawn PK, McLaughlin RA, Sampson DD, Eastwood PR, Hillman DR, Mitchell HW, Noble PB. Does smooth muscle in an intact airway undergo length adaptation during a

sustained change in transmural pressure? Journal of applied physiology. 2015; 118:533–543. [PubMed: 25729015]

11. Nadkarni SK, Pierce MC, Park BH, de Boer JF, Whittaker P, Bouma BE, Bressner JE, Halpern E, Houser SL, Tearney GJ. Measurement of collagen and smooth muscle cell content in atherosclerotic plaques using polarization-sensitive optical coherence tomography. Journal of the American College of Cardiology. 2007; 49:1474–1481. [PubMed: 17397678]
12. Lei M, Ghezzo H, Chen MF, Eidelman DH. Airway smooth muscle orientation in intraparenchymal airways. Journal of applied physiology. 1997; 82:70–77. [PubMed: 9029200]
13. Villiger M, Zhang EZ, Nadkarni SK, Oh WY, Vakoc BJ, Bouma BE. Spectral binning for mitigation of polarization mode dispersion artifacts in catheter-based optical frequency domain imaging. Optics express. 2013; 21:16353–16369. [PubMed: 23938487]
14. Zhang EZ, Vakoc BJ. Polarimetry noise in fiber-based optical coherence tomography instrumentation. Optics express. 2011; 19:16830–16842. [PubMed: 21935044]
15. Wang, RK., Tuchin, VV. Handbook of Coherent-Domain Optical Methods: Biomedical Diagnostics, Environmental Monitoring, and Materials Science. Tuchin, VV., editor. Springer New York; New York, NY: 2013. p. 665-742.
16. Hsiung PL, Nambiar PR, Fujimoto JG. Effect of tissue preservation on imaging using ultrahigh resolution optical coherence tomography. Journal of biomedical optics. 2005; 10:064033. [PubMed: 16409098]
17. Noble PB, Pascoe CD, Lan B, Ito S, Kistemaker LE, Tatler AL, Pera T, Brook BS, Gosens R, West AR. Airway smooth muscle in asthma: linking contraction and mechanotransduction to disease pathogenesis and remodelling. Pulmonary pharmacology & therapeutics. 2014; 29:96–107. [PubMed: 25062835]
18. James A, Carroll N. Airway smooth muscle in health and disease; methods of measurement and relation to function. The European respiratory journal. 2000; 15:782–789. [PubMed: 10780774]
19. Bai TR, Cooper J, Koelmeyer T, Pare PD, Weir TD. The effect of age and duration of disease on airway structure in fatal asthma. American journal of respiratory and critical care medicine. 2000; 162:663–669. [PubMed: 10934103]
20. Ma X, Cheng Z, Kong H, Wang Y, Unruh H, Stephens NL, Laviolette M. Changes in biophysical and biochemical properties of single bronchial smooth muscle cells from asthmatic subjects. American journal of physiology Lung cellular and molecular physiology. 2002; 283:L1181–1189. [PubMed: 12388349]
21. Gillis JM, Cao ML, Godfraind-De Becker A. Density of myosin filaments in the rat anococcygeus muscle, at rest and in contraction. II. Journal of muscle research and cell motility. 1988; 9:18–29. [PubMed: 3392185]
22. Godfraind-De Becker A, Gillis JM. Analysis of the birefringence of the smooth muscle anococcygeus of the rat, at rest and in contraction. I. Journal of muscle research and cell motility. 1988; 9:9–17. [PubMed: 3392188]
23. Smolensky AV, Ford LE. Filament lattice changes in smooth muscle assessed using birefringence. Canadian journal of physiology and pharmacology. 2005; 83:933–940. [PubMed: 16333365]
24. Smolensky AV, Ragozzino J, Gilbert SH, Seow CY, Ford LE. Length-dependent filament formation assessed from birefringence increases during activation of porcine tracheal muscle. The Journal of physiology. 2005; 563:517–527. [PubMed: 15618272]
25. Gray PR, Mitchell HW. Effect of diameter on force generation and responsiveness of bronchial segments and rings. The European respiratory journal. 1996; 9:500–505. [PubMed: 8730010]
26. Mitchell HW, Cvetkovski R, Sparrow MP, Gray PR, McFawn PK. Concurrent measurement of smooth muscle shortening, lumen narrowing and flow to acetylcholine in large and small porcine bronchi. The European respiratory journal. 1998; 12:1053–1061. [PubMed: 9863996]
27. Abramson MJ, Puy RM, Weiner JM. Allergen immunotherapy for asthma. Cochrane Database Syst Rev. 2003:CD001186. [PubMed: 14583928]
28. Chakir J, Haj-Salem I, Gras D, Joubert P, Beaudoin EL, Biardel S, Lampron N, Martel S, Chanez P, Boulet LP, Laviolette M. Effects of Bronchial Thermoplasty on Airway Smooth Muscle and Collagen Deposition in Asthma. Ann Am Thorac Soc. 2015; 12:1612–1618. [PubMed: 26325484]

29. Denner DR, Doeing DC, Hogarth DK, Dugan K, Naureckas ET, White SR. Airway Inflammation after Bronchial Thermoplasty for Severe Asthma. Ann Am Thorac Soc. 2015; 12:1302–1309. [PubMed: 26230374]
30. Reddel HK, Taylor DR, Bateman ED, Boulet LP, Boushey HA, Busse WW, Casale TB, Chanez P, Enright PL, Gibson PG, Jongste JC de, Kerstjens HA, Lazarus SC, Levy ML, O'Byrne PM, Partridge MR, Pavord ID, Sears MR, Sterk PJ, Stoloff SW, Sullivan SD, Szefler SJ, Thomas MD, Wenzel SE, C. American Thoracic Society/European Respiratory Society Task Force on Asthma. Exacerbations, An official American Thoracic Society/European Respiratory Society statement: asthma control and exacerbations: standardizing endpoints for clinical asthma trials and clinical practice. American journal of respiratory and critical care medicine. 2009; 180:59–99. [PubMed: 19535666]
31. Yun SH, Tearney GJ, Vakoc BJ, Shishkov M, Oh WY, Desjardins AE, Suter MJ, Chan RC, Evans JA, Jang IK, Nishioka NS, de Boer JF, Bouma BE. Comprehensive volumetric optical microscopy in vivo. Nat Med. 2006; 12:1429–1433. [PubMed: 17115049]
32. Yun S, Tearney G, de Boer J, Bouma B. Removing the depth-degeneracy in optical frequency domain imaging with frequency shifting. Optics express. 2004; 12:4822–4828. [PubMed: 19484034]
33. Park B, Pierce M, Cense B, de Boer J. Real-time multi-functional optical coherence tomography. Optics express. 2003; 11:782–793. [PubMed: 19461791]
34. Villiger M, Zhang EZ, Nadkarni SK, Oh WY, Vakoc BJ, Bouma BE. Spectral binning for mitigation of polarization mode dispersion artifacts in catheter-based optical frequency domain imaging. Optics express. 2013; 21:16353–16369. [PubMed: 23938487]
35. Gordon JP, Kogelnik H. PMD fundamentals: polarization mode dispersion in optical fibers. Proceedings of the National Academy of Sciences of the United States of America. 2000; 97:4541–4550. [PubMed: 10781059]
36. Zhang J, Guo S, Jung W, Nelson J, Chen Z. Determination of birefringence and absolute optic axis orientation using polarization-sensitive optical coherence tomography with PM fibers. Optics express. 2003; 11:3262–3270. [PubMed: 19471453]
37. Hitzenberger C, Goetzinger E, Sticker M, Pircher M, Fercher A. Measurement and imaging of birefringence and optic axis orientation by phase resolved polarization sensitive optical coherence tomography. Optics express. 2001; 9:780–790. [PubMed: 19424315]
38. Kemp N, Zaatari H, Park J, Rylander HG Iii, Milner T. Depth-resolved optic axis orientation in multiple layered anisotropic tissues measured with enhanced polarization-sensitive optical coherence tomography (EPS-OCT). Optics express. 2005; 13:4507–4518. [PubMed: 19495365]
39. Braaf B, Vermeer KA, de Groot M, Vienola KV, de Boer JF. Fiber-based polarization-sensitive OCT of the human retina with correction of system polarization distortions. Biomedical optics express. 2014; 5:2736–2758. [PubMed: 25136498]
40. Marvdashti T, Duan L, Lurie KL, Smith GT, Ellerbee AK. Quantitative measurements of strain and birefringence with common-path polarization-sensitive optical coherence tomography. Optics letters. 2014; 39:5507–5510. [PubMed: 25360914]

## One Sentence Summary

Birefringence microscopy platform provides images and volumetric assessments of airway smooth muscle structure and function in living subjects, and quantifies airway smooth muscle remodeling in mild asthmatic subjects.

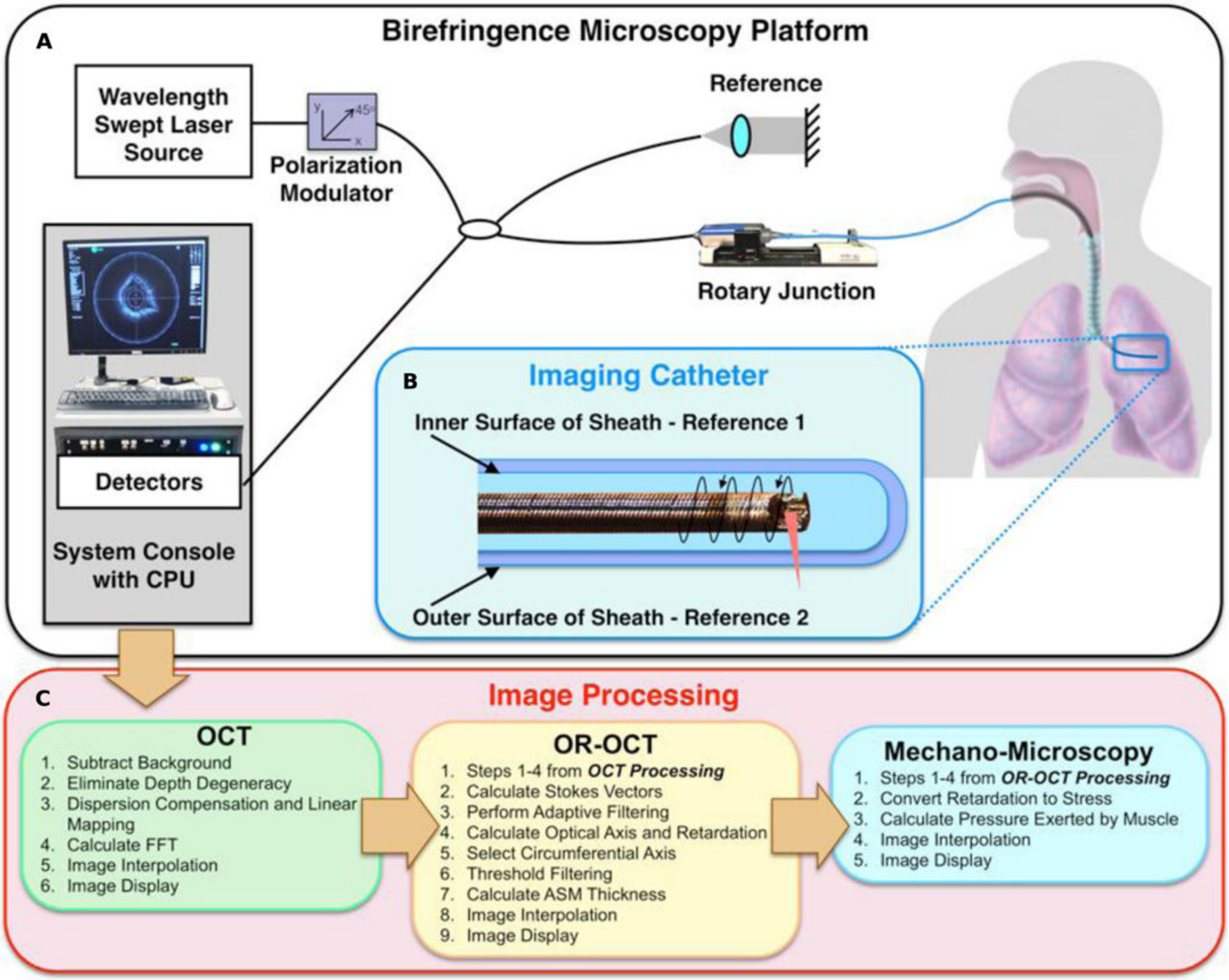

**Fig 1. Birefringence Microscopy Platform schematic**

**(A)** A schematic of the Birefringence Microscopy Platform. The fiber-based imaging system utilizes a wavelength swept-source. **(B)** Depiction of the endoscopic imaging catheter. A ball lens was made from a fiber tip and was angle polished for side-viewing. The imaging pitch is determined by the ratio of the rotation rate to pullback speed, and a dual-layer torque coil protects the imaging fiber and allows for rotation with minimal distortion. The inner and outer surfaces of the birefringent polymer sheath are used to obtain the reference orientation for *in vivo* OR-OCT imaging. **(C)** Outline of the processing steps used for obtaining OCT, OR-OCT, and Mechano-Microscopy images. A complete description of the components and processing can be found in the Supplementary Materials.

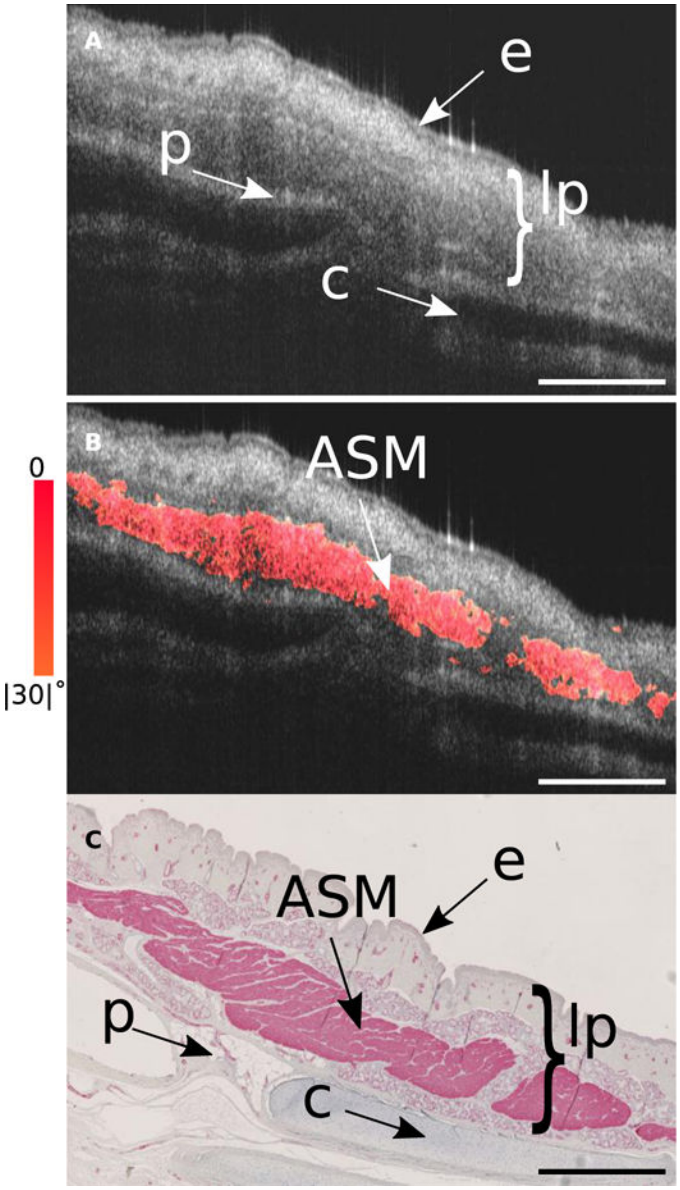

**Fig. 2. Segment of pig trachea where smooth muscle connects two cartilage plates**

**(A)** Structural OCT image of a segment of swine trachea that includes trachealis muscle. This segment of tissue was bisected and removed from the remaining trachea and was imaged using a bench-top scanner with the circumferential axis oriented in line with the primary image-scanning axis (see Fig. S7 - inset for bisection schematic). Features such as the epithelium, lamina propria, perichondrium, and cartilage rings are well defined, but the smooth muscle is often indistinguishable from surrounding glandular and connective tissue. **(B)** Using our birefringence microscopy platform we are able to separate out the circumferentially oriented (+/− 30°) birefringent tissue that corresponds to the smooth muscle. **(C)** The OCT image was matched to histology stained with alpha smooth muscle actin (αSMA). Comparison between the OR-OCT image and the αSMA stained histology reveals the high degree of isolation and sensitivity our platform is capable of for identifying smooth muscle. *lp*, lamina propria; *e*, epithelium; *p*, perichondrium; *c*, cartilage. Scale bars, 500 µm.

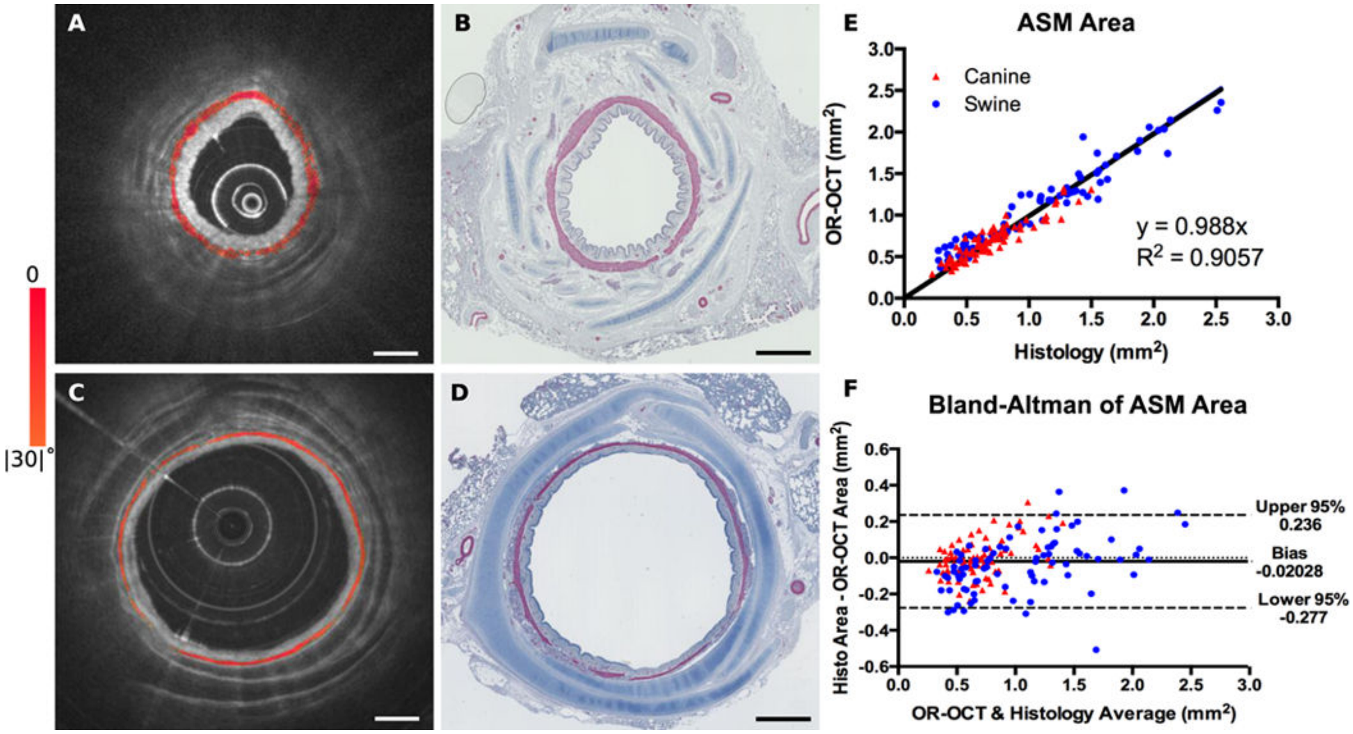

**Fig. 3. ASM assessment validation with histology**

**(A)** OR-OCT image depicting the cross section of a canine bronchiole. **(B)** The corresponding histology match, stained with αSMA antibody. The slide was digitized at 5× magnification. **(C,D)** OR-OCT image and matching histology from a swine bronchiole, obtained in the same manner as described for the canine match. **(E)** Assessments obtained with OR-OCT compared with those from histology. **(F)** Bland-Altman plot of the same data, indicating minimal bias in our measurements. The data is comprised of 162 OCT-histology image pairs, including 82 paired images obtained from 17 segments of swine bronchi ranging in diameter from 3–7mm, and 80 paired images obtained from 17 segments of canine bronchi ranging in diameter from 2–5mm. Scale bars, 1mm.

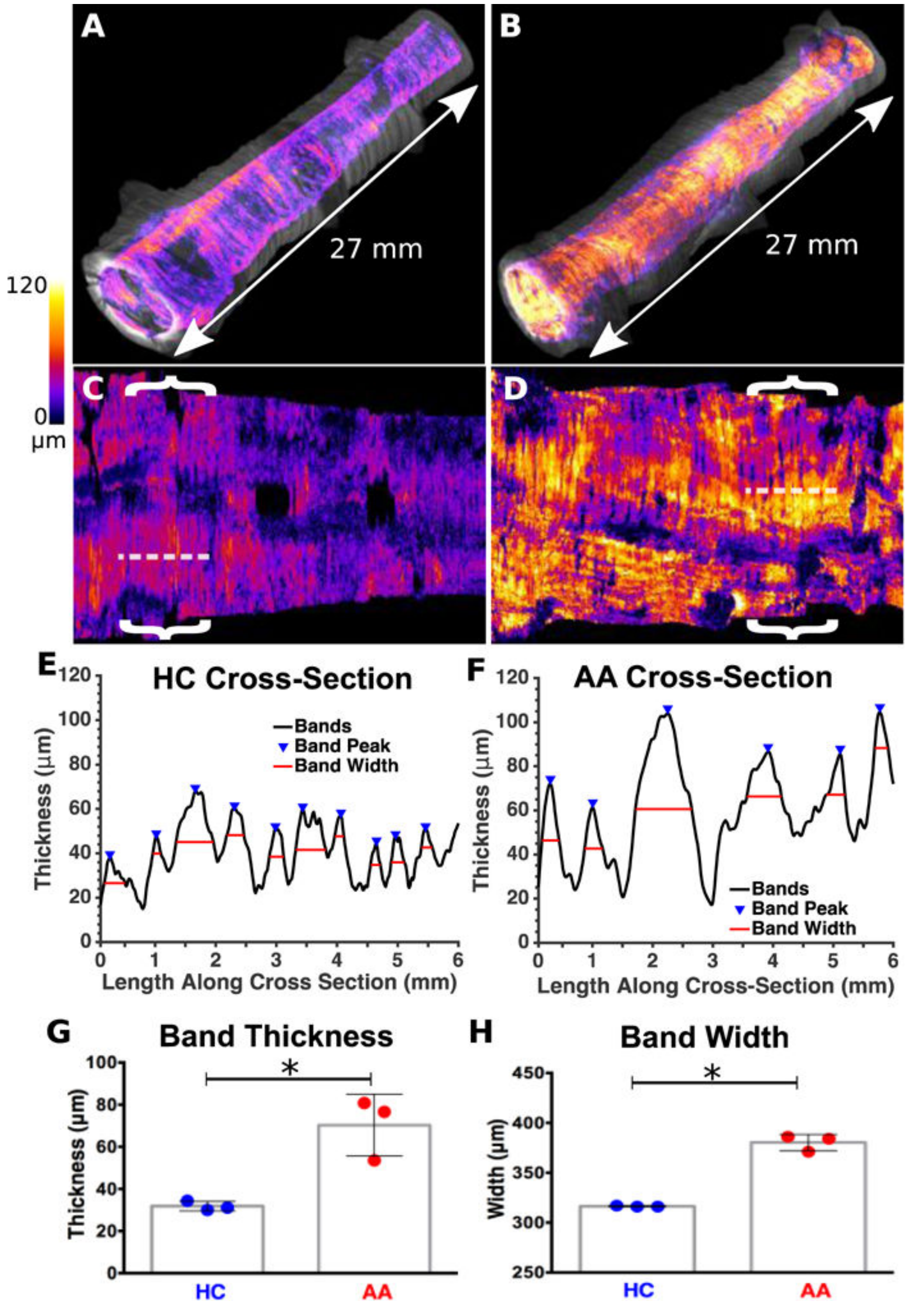

**Fig. 4. Morphological comparison between asthmatic and healthy control human subjects, *in vivo***

**(A,B)** Circularized volumetric image from a 2.7 cm endoscopic pullback of a **(A)** healthy control (HC) and a **(B) allergic** asthmatic (AA) subject, acquired from similar regions in the right upper lobe. ASM thickness was encoded in color according to the scale provided, and was overlaid on the grayscale structural OCT images in order to generate the volume renderings. **(C,D)** Unwrapped and two dimensional representations of the airway segments depicted in (*A,B*). **(E)** Thickness profile from a 6 mm longitudinal cross section of the non-asthmatic bronchus (obtained from the region indicated with a dashed line in **(C)**). **(F)** Comparable profile from the asthmatic bronchus (region indicated with dashed line in **(D)**).

**(G)** Comparison of average ASM thickness obtained from a series of comparable cross-sections (indicated for the two datasets shown with brackets) in 3 healthy control and 3 allergic asthmatic segments (35.9 µm, +/− 4.28 µm for healthy control versus 70.3 µm +/− 14.7 µm for allergic asthmatic; $P < 0.05$). **(H)** Comparison of Column graph comparing ASM band widths obtained from the same cross-sections (331.7 µm +/− 13.65 µm for healthy control versus 380.3 µm +/− 8.145 µm for allergic asthmatic; $P < 0.05$). The data graphed in (*G,H*) was obtained from a 6 mm airway segment of similar diameter in each individual imaged. Dashed lines and brackets, 6 mm.

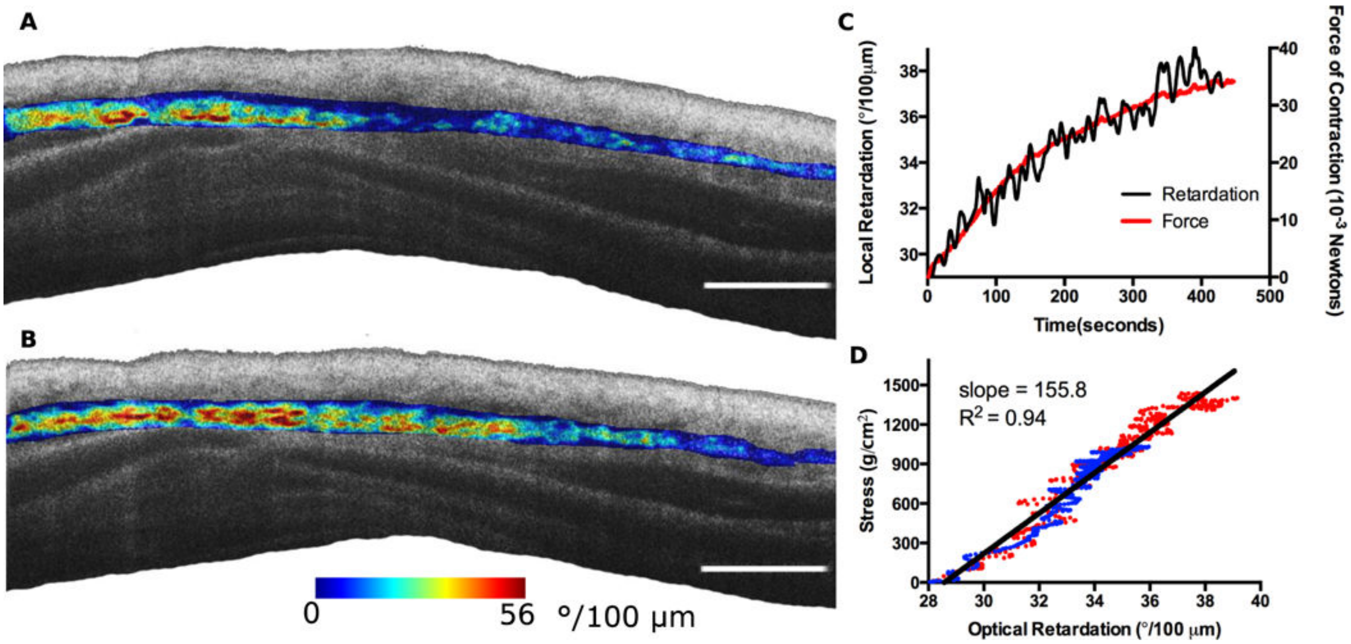

**Fig. 5. Stimulated contraction of tracheal smooth muscle strips**

A segment of swine trachea containing the trachealis muscle was dissected and pinned at the cartilage plates to a force transducer just above and below where the muscle connects to the cartilage. Contraction was induced by the application of acetyl methacholine to the epithelial surface of the tracheal segment and mechano-microscopy images were acquired continuously alongside the recorded force data. **(A,B)** Mechano-microscopy images depicting the local retardation of the segmented muscle overlaid on the structural image. The initial time point, immediately following the application of methacholine **(A)**, is shown along with the time point corresponding to the peak contractile state **(B)**. **(C)** Time evolution of contraction in terms of force (red, dashed) and local retardation (black, solid). The local retardation data points were obtained by taking the mean local retardation in a given frame of all pixels identified as being smooth muscle. The results were averaged over 5 second intervals. **(D)** Adjustment of the force curve relative to the estimated muscle volume of the sample. The two plotted datasets (blue and red) correspond to the two samples. Scale bars, 100 μm.

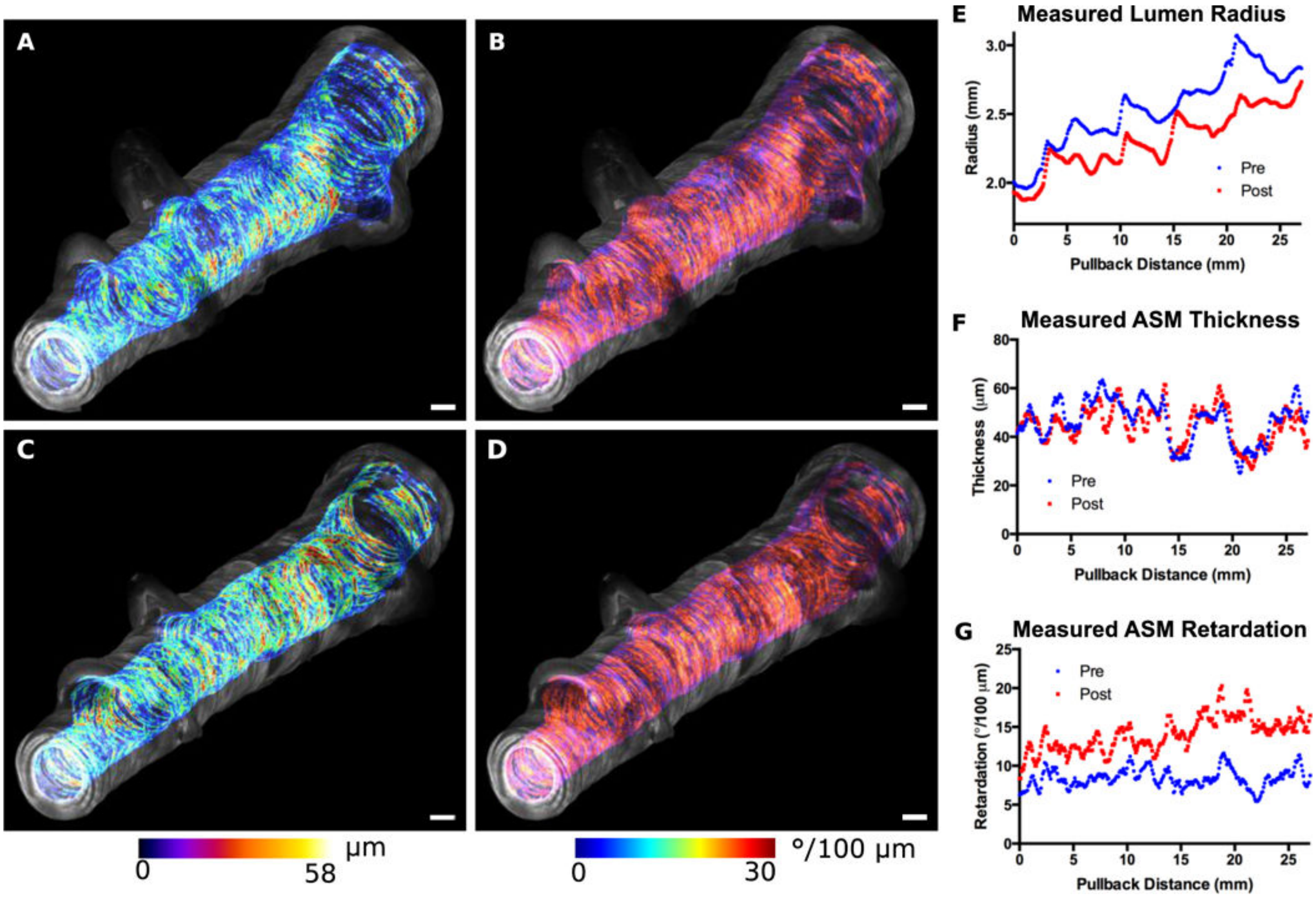

**Fig. 6. Relaxed and contracted states for a length of swine bronchus**

A 2.7 cm *ex vivo* segment was imaged before **(A,B)** and three minutes after **(C,D)** the application of methacholine. Optical retardation *(A,C)* and ASM thickness *(B,D)* were color encoded according to the scales provided and were overlaid on the grayscale structural OCT images in order to generate the volume renderings displayed. **(E–G)** Plots of parameters (pre- and post-methacholine per matched frame along the entire segment. The airway radius **(E)**, ASM thickness **(F)**, and ASM local retardation **(G)** were plotted along the length of the airway. Mean percent changes (averaged over entire segment) are as follows: area −8.9%; thickness −0.9%; local retardation +73.4%. Scale bars, 1mm.